chain of IgG antibody released from the co-gel was much larger in Group 2 where non-treated anti-BSA antibody was simply mixed in a ST-gelatin gel than that in Group 3. This result indicates that the amount of ST-Ab released from a co-gel is reduced, indicating that anti-BSA ST-Ab is copolymerized with ST-gelatin to form a copolymerized gel. SEM observation revealed that the co-gel of ST-gelatin and ST-Ab was found to form gelatinous network meshes, which was composed of approximately one-hundred-nanometer-scale fibers, globules, and open-structured interconnecting microvoids or channels at the surface and interior regions (Fig. 2B).

3.2. Permeation of antigen into gels

To determine whether the copolymerized gel composed of anti-BSA ST-Ab and ST-gelatin inhibits or retards BSA permeation, rhodamine-conjugated BSA solution was pored over the disks, and time-development cross-sectional permeation characteristics were visually and quantitatively monitored by a CLSM. As shown in Fig. 5A, irrespective of the groups, BSA tended to localize on the surface region of the gels at an early period of immersion, followed by its gradual permeation into the interior of the gels and into deeper regions with time. However, the permeation in Group 3 (the co-gel of ST-Ab and ST-gelatin) was the slowest among three groups, and the co-gel in Group 3 appeared to trap a dye-conjugated BSA. On the other hand, there was no significant difference in permeation characteristics between Groups 1 and 2. After a long time, dye-conjugated BSA homogeneously distributed all over the gel. This was quantitatively determined from the depth profile of fluorescence intensity from the surface, as shown in Fig. 5B. In Group 3, permeated BSA molecules were limited in the surface region after a 36-h permeation period and were still mostly localized and limited in surface-to-subsurface regions even after a 60-h permeation period, as compared with the other two groups in which there was high accumulation in surface-to-subsurface regions and homogeneous distribution in deeper regions. This characteristic is derived from a concentration-dependent phenomenon; at a high BSA concentration relative to the immobilized antibody concentration, the majority of non-complexed BSA permeated through the gel, and at a low BSA concentration, immuno-complex is formed and localized at the surface region (data not shown). This means that a sufficient amount of antibody relative to the permeating antigen is necessary to prevent permeation of its antigen into a tissue.

3.3. Invasion assay

To determine whether the co-gel of ST-gelatin and anti-HGF ST-Ab inhibits HGF permeation, an invasion assay using pancreatic cancer cells (SUIT-2) was performed with 10 mg each of the photocured gels [Group 1, gel prepared from ST-gelatin (30 wt%); Group 2, ST-gelatin (30 wt%) and non-treated anti-HGF antibody (0.2 wt%); or Group 3, ST-gelatin (30 wt%) and anti-HGF ST-Ab (0.2 wt%)], as shown in Fig. 6A. As shown in Fig. 6B, without the gel layer system (control: Group 0) and with the simple ST-gelatin gel layer system (Group 1), the numbers of invaded cells markedly increased with the addition of HGF, regardless of HGF concentration. There was negligible difference in the number of invaded cells between these two groups at respective HGF concentration. On the other hand, the numbers of invaded cells in Groups 2 and 3 were suppressed in spite of the addition of HGF and a markedly suppressive effect on invasion was noted especially at a low concentration (10 ng/ml). These findings indicate that HGF is neutralized by anti-HGF antibody in the gel regardless of free non-treated anti-HGF antibody or fixed anti-HGF ST-Ab.

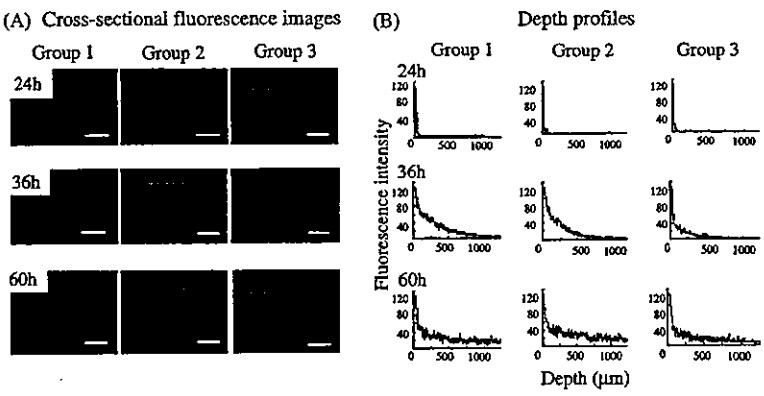

Fig. 5. The permeation of rhodamine-conjugated BSA into three different gels [Group 1, ST-gelatin (30 wt%); Group 2, ST-gelatin (30 wt%) and non-treated anti-BSA antibody (0.2 wt%); or Group 3, ST-gelatin (30 wt%) and anti-BSA ST-Ab (0.2 wt%)] was observed by a CLSM. (A) Cross-sectional fluorescence images. Bar: 500 μm. (B) Depth profiles (fluorescence intensity as a function of the distance from the gel surface).

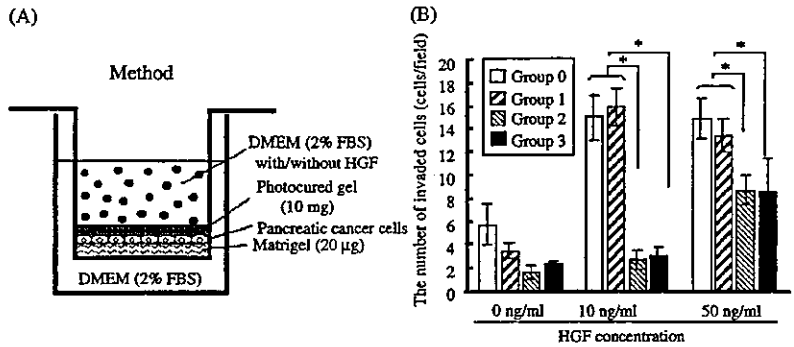

Fig. 6. Invasion assay was performed with modifications using 10 mg each of the three kinds of photocured gelatin gels [Group 1, ST-gelatin (30 wt%) only; Group 2, ST-gelatin (30 wt%) and non-treated anti-human HGF antibody (0.2 wt%); or Group 3, ST-gelatin (30 wt%) and anti-human HGF ST-Ab (0.2 wt%)]. ($n = 3$) In the control group, a gel was not used. ($n = 3$) Statistical analysis was performed using analysis of variance (ANOVA). Post-hoc comparisons were made by the Scheffe analysis. Differences were considered significant at $p < 0.05$. In Groups 0 and 1, the numbers of invaded SUIT-2 cells increased with the addition of HGF. On the other hand, in Groups 2 and 3, HGF-dependent invasion of SUIT-2 cells was significantly suppressed. $^{*}p < 0.05$.

4. Discussion

We newly prepared ST-Ab with a minimal loss of its affinity to antigen, which was copolymerized with ST-gelatin to produce a tissue-adhesive co-gel of ST-gelatin and ST-Ab (Fig. 2A). Our previous studies showed that ST-gelatin can serve as an in situ formable and bioactive-substance-immobilizable matrix upon photopolymerization to produce a gel under visible-light irradiation, which adheres well on surgically resected tissues [26–28]. When a non-treated anti-BSA antibody was immobilized in the ST-gelatin gel, antibody was released from the gel, whereas a mixture of anti-BSA ST-Ab and ST-gelatin formed a copolymerized gel upon visible-light irradiation, from which ST-Ab was less released from the gel (Fig. 4). In addition, the depth profile analysis of the distribution of the dye-conjugated BSA as an antigen in the gel clearly showed limited or retarded permeation of antigen into the co-gel of ST-Ab and ST-gelatin at an early period (Fig. 5). These findings imply that the co-gel using ST-Ab works as an antigen-barrier, which prevents local antigen permeation into a target tissue coated with a gel.

In an in vitro invasion assay, the inhibitory potential for HGF-dependent invasion was observed in Groups 2 (ST-gelatin + non-treated anti-HGF antibody) and 3 (ST-gelatin + anti-HGF ST-Ab) at almost the same extent (Fig. 6B). The inhibitory effect was dose-dependent, and more profound at a low HGF concentration. Combined with the result of BSA permeation experiment determined by a CLSM, it is highly anticipated that a sufficiently large amount of antibody immobilized or chemically bound in a tissue-adhesive gel completely blocks HGF activity into resected tissues.

An antibody immobilization approach is beneficial in terms of ease in preparation of an immobilized gel (Fig. 1B), but its shortcoming is that antibodies may diffuse from a gel and transfer to distant site, resulting in gradual decrease of local concentration of antibody. On the other hand, an antibody-bound approach (Fig. 1C) does not have such a shortcoming because an antibody is fixed by polymerization in the gel.

The proposed strategy may be a promising cytostatic approach for cancer therapy, which minimizes migration and proliferation of remnant cancer cells as a cytokine-barrier. If needed, anti-EGF, anti-bFGF, anti-VEGF and anti-TGF-β antibodies could be styrenated in the same manner, and copolymerized with ST-gelatin to produce a co-gel. When a cytotoxic substance, such as an anti-cancer drug, was immobilized in a co-gel of ST-gelatin and anti-cytokine ST-Ab and continuously released from a co-gel to a target tissue (Fig. 1D) [28], its synergetic effect derived from combined cytostatic and cytotoxic approaches could bring in a powerful therapeutic outcome without serious systemic adverse effects.

5. Conclusions

ST-Ab newly prepared was copolymerized with ST-gelatin to produce a tissue-adhesive co-gel, which may act as antigen-barrier. When anti-cytokine antibody was fixed in a gel, the cytokine, produced in surgical procedure and accumulated in the peritoneal fluid, was captured by or complexed with its antibody in a gel, resulting in prevention of the permeation of the cytokine into the resected tissue. Such local antibody therapy may help inhibit malignant behavior of remnant cancer cells without retarded wound healing at distant sites.

Acknowledgements

This study is financially supported by Promotion Fundamental Studies in Health Science of the Organization for Pharmaceutical Safety and Research (OPSR, contract grant number: 97-15) and Grant-in-Aid for Scientific Research from Ministry of Education, Culture, Sports, Science, and Technology of Japan (contract grant number: A2-12358017 and B2-12470277). The authors wish to thank K. Yasutake for excellent technical assistance.

References

[1] Yapp DT, Lloyd DK, Zhu J, Lehnert SM. Cisplatin delivery by biodegradable polymer implant is superior to systemic delivery by osmotic pump or i.p. injection in tumor-bearing mice. Anticancer Drugs 1998;9:791–6.
[2] Tamura T, Fujita F, Tanimoto M, Koike M, Suzuki A, Fujita M, Horikiri Y, Sakamoto Y, Suzuki T, Yoshino H. Anti-tumor effect of intraperitoneal administration of cisplatin-loaded microspheres to human tumor xenografted nude mice. J Control Rel 2002;80: 295–307.
[3] St'astny M, Plocova D, Etrych T, Kovar M, Ulbrich K, Rihova B. HPMA-hydrogels containing cytostatic drugs. Kinetics of the drug release and in vivo efficacy. J Control Rel 2002;81: 101–11.
[4] Lee CM, Tanaka T, Murai T, Kondo M, Kimura J, Su W, Kitagawa T, Ito T, Matsuda H, Miyasaka M. Novel chondroitin sulfate-binding cationic liposomes loaded with cisplatin efficiently suppress the local growth and liver metastasis of tumor cells in vivo. Cancer Res 2002;62:4282–8.
[5] Cienfuegos JA, Manuel FA. Analysis of intraoperative radiotherapy for pancreatic carcinoma. Eur J Surg Oncol 2000;26:S13–5.
[6] Takeda S, Inoue S, Kaneko T, Harada A, Nakao A. The role of adjuvant therapy for pancreatic cancer. Hepatogastroenterology 2001;48:953–6.
[7] Sperti C, Pasquali C, Piccoli A, Pedrazzoli S. Recurrence after resection for ductal adenocarcinoma of the pancreas. World J Surg 1997;21:195–200.
[8] Hofer SO, Molema G, Hermens RA, Wanebo HJ, Reichner JS, Hoekstra HJ. The effect of surgical wounding on tumour development. Eur J Surg Oncol 1999;25:231–43.
[9] Di Renzo MF, Poulsom R, Olivero M, Comoglio PM, Lemoine NR. Expression of the Met/hepatocyte growth factor receptor in human pancreatic cancer. Cancer Res 1995;55:1129–38.
[10] Ebert M, Yokoyama M, Friess H, Buchler MW, Korc M. Coexpression of the c-met proto-oncogene and hepatocyte growth factor in human pancreatic cancer. Cancer Res 1994;54:5775–8.
[11] Jiang W, Hiscox S, Matsumoto K, Nakamura T. Hepatocyte growth factor/scatter factor, its molecular, cellular and clinical implications in cancer. Crit Rev Oncol Hematol 1999;29:209–48.
[12] Matsumoto K, Date K, Ohmichi H, Nakamura T. Hepatocyte growth factor in lung morphogenesis and tumor invasion: role as a mediator in epithelium-mesenchyme and tumor-stroma interactions. Cancer Chemother Pharmacol. 1996;38:S42–7.
[13] Date K, Matsumoto K, Kuba K, Shimura H, Tanaka M, Nakamura T. Inhibition of tumor growth and invasion by a four-kringle antagonist (HGF/NK4) for hepatocyte growth factor. Oncogene 1998;17:3045–54.
[14] Date K, Matsumoto K, Shimura H, Tanaka M, Nakamura T. HGF/NK4 is a specific antagonist for pleiotrophic actions of hepatocyte growth factor. FEBS Lett 1997;420:1–6.
[15] Kuba K, Matsumoto K, Ohnishi K, Shiratsuchi T, Tanaka M, Nakamura T. Kringle 1-4 of hepatocyte growth factor inhibits proliferation and migration of human microvascular endothelial cells. Biochem Biophys Res Commun 2000;279:846–52.
[16] Kuba K, Matsumoto K, Date K, Shimura H, Tanaka M, Nakamura T. HGF/NK4, a four-kringle antagonist of hepatocyte growth factor, is an angiogenesis inhibitor that suppresses tumor growth and metastasis in mice. Cancer Res 2000;60:6737–43.
[17] Maehara N, Matsumoto K, Kuba K, Mizumoto K, Tanaka M, Nakamura T. NK4, a four-kringle antagonist of HGF, inhibits spreading and invasion of human pancreatic cancer cells. Br J Cancer 2001;84:864–73.
[18] Kimura F, Miyazaki M, Suwa T, Kadoyama C, Itoh H, Ambiru S, Shimizu H, Nakagawa K. Correlation between human hepatocyte growth factor and interleukin-6 concentrations after surgery. Hepatogastroenterology 1999;46:1030–5.
[19] Kimura F, Miyazaki M, Suwa T, Kakizaki S, Itoh H, Kaiho T, Ambiru S, Shimizu H, Togawa A. Increased levels of human hepatocyte growth factor in serum and peritoneal fluid after partial hepatectomy. Am J Gastroenterol 1996;91:116–21.
[20] Miyata K, Taniguchi H, Tsubouchi H, Daikuhara Y, Takahashi T. Levels of human hepatocyte growth factor (hHGF) in peritoneal fluid after partial hepatectomy. Hepatogastroenterology 1996;43:1594–600.
[21] von Schweinitz D, Faundez A, Teichmann B, Birnbaum T, Koch A, Hecker H, Gluer S, Fuchs J, Pietsch T. Hepatocyte growth-factor-scatter factor can stimulate post-operative tumor-cell proliferation in childhood hepatoblastoma. Int J Cancer 2000;85:151–9.
[22] Zagury D, Le Buanec H, Bizzini B, Burny A, Lewis G, Gallo RC. Active versus passive anti-cytokine antibody therapy against cytokine-associated chronic diseases. Cytokine Growth Factor Rev 2003;14:123–37.
[23] Gordon MS, Margolin K, Talpaz M, Sledge Jr GW, Holmgren E, Benjamin R, Stalter S, Shak S, Adelman D. Phase I safety and pharmacokinetic study of recombinant human anti-vascular endothelial growth factor in patients with advanced cancer. J Clin Oncol 2001;19:843–50.
[24] Ferrara N. Role of vascular endothelial growth factor in physiologic and pathologic angiogenesis: therapeutic implications. Semin Oncol 2002;29:S10–4.
[25] Herbst RS, Shin DM. Monoclonal antibodies to target epidermal growth factor receptor-positive tumors: a new paradigm for cancer therapy. Cancer 2002;94:1593–611.
[26] Okino H, Nakayama Y, Tanaka M, Matsuda T. In situ hydrogelation of photocurable gelatin and drug release. J Biomed Mater Res 2002;59:233–45.
[27] Okino H, Manabe T, Tanaka M, Matsuda T. Novel therapeutic strategy for prevention of malignant tumor recurrence after surgery: local delivery and prolonged release of adenovirus immobilized in photocured, tissue-adhesive gelatinous matrix. J Biomed Mater Res 2003;66:643–51.
[28] Okino H, Maeyama R, Manabe T, Matsuda T, Tanaka M. Transtissue, sustained-release of gemcitabine from photocured gelatin gel inhibits the growth of heterotopic human pancreatic tumor in nude mice. Clin Cancer Res 2003;9:5768–93.
[29] Matsuda T, Magoshi T. Preparation of vinylated polysaccharides and photofabrication of tubular scaffolds as potential use in tissue engineering. Biomacromolecules 2002;3:942–50.
[30] Iwamura T, Katsuki T, Ide K. Establishment and characterization of a human pancreatic cancer cell line (SUIT-2) producing carcinoembryonic antigen and carbohydrate antigen 19-9. Jpn J Cancer Res 1987;78:54–62.

Available online at www.sciencedirect.com
SCIENCE DIRECT®
Biomaterials 26 (2005) 1675–1684
Biomaterials
www.elsevier.com/locate/biomaterials

Photo-polymerized microarchitectural constructs prepared by microstereolithography (μSL) using liquid acrylate-end-capped trimethylene carbonate-based prepolymers

Il Keun Kwon, Takehisa Matsuda*

Division of Biomedical Engineering, Graduate School of Medicine, Kyushu University, 3-1-1 Maidashi, Higashi-ku, Fukuoka 812-8582, Japan

Received 2 April 2004; accepted 25 June 2004
Available online 20 August 2004

Abstract

Precision microarchitectural constructs made of acrylated trimethylene carbonate (TMC)-based liquid prepolymers were photo-polymerized using a custom-designed microstereolithographic apparatus. In this study, three different photo-polymerizable liquid prepolymers were prepared by the polymerization of TMC with a low molecular weight poly(ethylene glycol) (PEG) (mol. wt. 200 or 1000); designated as PEG200 or PEG1000, respectively or trimethylolpropane (TMP) as an initiator, and subsequently end-capped with an acrylate group. As a result of layer-by-layer photo-irradiation of the prepolymer with a movable ultraviolet light pen driven by computer-aided design, a three-dimensional (3D) micropillar array, a microbank array, a microcone array, and multi-microtunnels formed on a platform plate or a glass plate were precisely fabricated. The PEG-based polymers exhibited a very low cell adhesion potential, whereas the TMP-based hydrophobic polymer exhibited high cell adhesion and proliferation potentials. The microbank array, which consisted of a plate made of the TMP-based polymer and microbanks made of the PEG200-based polymer, caused cell adhesion and proliferation only on the plate. Upon the implantation of microcone arrays under the subcutis of rats, the photo-polymerized construct made of the poorly swellable PEG200-based polymer exhibited only surface erosion and limited drug loading and releasing potentials. On the other hand, the photo-polymerized construct made of the highly swellable PEG1000-based polymer exhibited not only surface erosion but also bulk erosion and high drug loading and releasing potentials. In this paper, we discuss their potential biomedical applications.

Keywords: Microstereolithography (μSL); Acrylated liquid prepolymer; Photo-polymerization; Microarchitectures; Degradation; Drug release

1. Introduction

Stereolithography (SL), a rapid photo-typing technique, allows the integral formation of three-dimensional (3D) constructs layer-by-layer photo-polymerization using computer-aided design (CAD)/computer-aided manufacturing (CAM) with an ultraviolet (UV) light pen and a photo-polymerizable liquid prepolymer [1–4]. Microstereolithographic (μSL) allows a precision macroshaping and microarchitecturing of a device or scaffold design, and surface architecture for advanced medical procedures [5–10].

To this end, the authors have been developing photo-polymerizable biodegradable liquid prepolymers and their photo-polymerization processes. Our previous studies showed that prepolymers, composed of ε-caprolactone (CL) and trimethylene carbonate (TMC), end-capped with photo-reactive groups, such as coumarin [11–14], phenylazide [15], or acrylate [16], are rapidly converted from liquid to solid upon photo-irradiation. Furthermore, μSL microarchitectures, such as microneedles, microcylinders, microbanks, and microlattices on a platform, were feasible using di-acrylated poly(CL/TMC) with a custom-designed μSL

*Corresponding author. Tel.: +81-92-642-6210; fax: +81-92-642-6212.
E-mail address: matsuda@med.kyushu-u.ac.jp (T. Matsuda).

0142-9612/$ - see front matter © 2004 Elsevier Ltd. All rights reserved.
doi:10.1016/j.biomaterials.2004.06.041

apparatus [17]. As an extension of a series of photo-polymerizable biodegradable liquid prepolymers, we very recently synthesized a series of acrylated biodegradable liquid TMC-based prepolymers, which were obtained by the polymerization of TMC with a low molecular weight PEG (mol. wt. 200 or 1000) or trimethylolpropane (TMP) as an initiator, and subsequently acrylate end-capped. The hydrolytical surface erosion of completely photo-polymerized films by visible-light irradiation in the presence of camphorquinone was thoroughly evaluated by a force-indentation technique using atomic force microscopy (AFM) [18]. The photo-polymerized films prepared from prepolymers with a low molecular weight PEG (PEG200) and TMP exhibited a much lower hydrolysis potential than polymers prepared from PEG1000-derived prepolymers in terms of weight loss, water uptake and swellability [18].

In this study, as an extension of our series of studies on μSL, various microarchitectures using three different TMC-based liquid prepolymers, previously prepared by us, were photo-polymerized using the custom-designed μSL system for prototype models, which can be translated to real tissue engineering scaffolds. As an application, photo-polymerized microarchitectural constructs (microarrays) consisted of a cell-adhesive plate and noncell-adhesive banks that were prepared for regiospecific 2D cell culture. For the 3D culture system, multi-microtunnel constructs were photo-polymerized. A multi-needle microarchitecture was photo-polymerized as a prototype model of sustained release of a drug in the deep region of a diseased tissue. The in vivo hydrolytic degradation behavior of photo-polymerized microcone constructs made of PEG-based polymers, and their drug loading and in vivo releasing potentials under the subcutis of rats were demonstrated (Fig. 1).

(A) **Acrylated prepolymer (TMC/PEG200)**

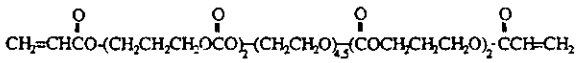

(B) **Acrylated prepolymer (TMC/PEG1k)**

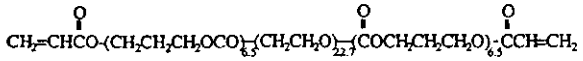

(C) **Acrylated prepolymer (TMC/TMP)**

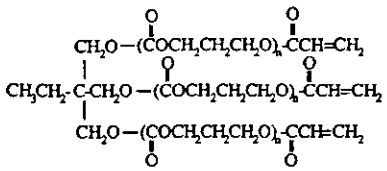

Fig. 1. Chemical structures of photo-polymerizable TMC-based liquid prepolymers derived from (A) PEG200, (B) PEG1000, and (C) TMP.

2. Materials and methods

2.1. General procedure

All solvents and reagents were purchased from either Wako Pure Chemical Industries, Ltd. (Osaka, Japan) or Sigma-Aldrich Japan, Inc. (Tokyo, Japan). TMC was prepared according to the method described in our previous paper and recrystallized from a mixed solvent of ethyl acetate and hexane [11]. TMP was recrystallized from acetone. PEG [mol. wt. of 200 or 1000, according to the manufacturer's information (Wako)] was purified by precipitation from cold hexane and subsequently vacuum-dried prior to use. Acryloyl chloride was used as obtained without further purification. Other solvents and reagents were purified by distillation. ^{1}H-NMR spectra were recorded on a JNM-AL300 system (JEOL, Tokyo, Japan). Chemical shifts are given in δ values from Me_4Si as an internal standard. The number-average molecular weight (M_n) of each prepolymer was determined by gel permeation chromatography (GPC), which was carried out on a high-performance liquid chromatograph (HPLC, JASCO-JMBS, Tokyo, Japan) equipped with a TSK-GEL column α-3000 (TOSOH, Tokyo, Japan) using PEG as a standard and tetrahydrofuran (THF) as an eluent. Viscosity of each prepolymer was determined by a cone-and-plate viscometer (TV-20, Tokisangyo Co. Ltd., Tokyo, Japan) with a rotational cone rotor (1°34′ × R24) under a shearing rate (1 rpm), a torque (5750 μN m) at 25 °C, and expressed as Pa s. UV irradiation was carried out using a 250-W mercury–xenon (Hg–Xe) lamp (Hamamatsu Photonics L5662-02, Shizuoka, Japan). The intensity of UV light was measured at 365 nm on TOPCON UVR-25 (Tokyo, Japan).

2.2. Synthesis of acrylate-end-capped prepolymer

A typical procedure for the preparation was as follows [18]. TMC-based oligomers were prepared using TMC as the monomer and PEG (mol. wt. 200 or 1000) or TMP as an initiator and tin(II)2-ethylhexanoate as a catalyst (feed molar ratios are shown in Table 1). The reaction was carried out for 4 h at 200 °C, followed by heating for 2 h at 160 °C in a flask in N_2 atmosphere. The resultant oligomer was dissolved in dichloromethane. Subsequently, an excess of acryloyl chloride was added to this flask in N_2 atmosphere and the reaction mixture was stirred for 8 h at 50 °C. The prepolymer was precipitated from excess hexane and vacuum-dried at 30 °C. The resultant prepolymer was viscous liquid at room temperature. Acrylate content was determined from peak intensities in the ^{1}H-NMR spectra relative to those of the vinyl group and PEG or TMP unit yielding the following results: ^{1}H-NMR (300 MHz, $CDCl_3$, ppm): $\delta = 2.05$ (multiplet), 3.65

Table 1
Acrylate-endcapped liquid TMC-based prepolymers

Prepolymer code	Initiator	Initial feed (molar ratio)	Acrylate end-capped prepolymer				Photo-polymerized film[a]	
			Composition[b]	Degree of acrylation[b] (%)	M_n[c]	Viscosity[d] (Pa s)	Receding contact angle[e]	DW[f]
		TMC: Iniator	TMC: Iniator					
T/P200	PEG200	1:0.250	1:0.250	90	8.0×10^2	1.3 ± 0.05	27 ± 3.56	2
T/P1k	PEG1000	1:0.076	1:0.076	97	2.4×10^3	2.1 ± 0.33	<5.0	30
T/TMP	$CH_3CH_2C(CH_2OH)_3$	1:0.167	1:0.167	92	1.1×10^3	2.6 ± 0.22	47.4 ± 5.33	1

[a]Photo-polymerizing conditions: liquid film of acrylated prepolymers (thickness; 0.2 mm). Photoirradiation at the intensity of 2 W/cm^2 at 365 nm for 1 min at room temperature.
[b]Molar ratio; determined by ^{1}H-NMR.
[c]Determined by GPC in THF (PEG standard). Mn: number-average molecular weight.
[d]Determined by a cone-plate viscometer using a rotational cone rotor (1° 34′ × R24): a shearing rate, 1 rpm; a torque, 5750 μN m, 25 °C ($n = 4$).
[e]Water contact angle measured by the sessile drop method ($n = 4$).
[f]The degree of water adsorptivity of photo-polymerized film after 2-day immersion in aqueous solution (see Eq. (1)).

(doublet), 4.24 (multiplet), 5.85 (doublet), 6.12 (quartet) and 6.42 (doublet).

2.3. UV-induced photo-polymerizing characteristics

Round liquid films (ϕ 10 mm) of the acrylated prepolymers were irradiated with the Hg–Xe lamp at a 2 W/cm^2. After the immersion of photo-polymerized films into excess dichloromethane to remove the soluble fraction, the insoluble polymers were dried and weighed. The gel content of the network was defined as the weight percentage of the insoluble part (W_g) with respect to that of the initial prepolymer (W): $W_g/W \times 100$.

2.4. Water contact angle

The surface wettability of photo-polymerized films was evaluated by measuring static contact angles toward deionized water using the sessile drop method with a contact angle meter (CA-D, Kyowa Interface Co. Ltd., Tokyo, Japan) at 25 °C.

2.5. Water adsorptivity

The photo-polymerized films were immersed for 2 days in an aqueous solution at 25 °C. The weight of swollen films (W_S) and that of dried films (W_D) were measured after wiping the surface with paper and vacuum drying, respectively. The degree of water adsorptivity (DW) was evaluated as

$$DW(\%) = 100 \times [W_S - W_D]/W_D. \quad (1)$$

2.6. Photo-polymerization using a μSL apparatus

A layer-by-layer photo-polymerization of microarchitectural constructs using a custom-designed μSL apparatus prepared in our previous study was carried out (Fig. 2) [17]. The μSL apparatus consisted of a movable light pen with a photo-mask (diameter, 50 μm), an optical fiber connecting the light pen and the light source (Hg–Xe lamp), a vertical elevator and controller (Sigma Koki MARK-41, Tokyo, Japan) driven by computer-assisted design, and a liquid prepolymer bath. The stage controller manipulated the movement of the light pen at a rate of 5 μm/s and photo-irradiation intensity was set at 2 W/cm^2 (365 nm wavelength), and the photo-polymerizable liquid prepolymer was refilled on the surface by lowering the vertical elevator table into the liquid prepolymer bath (200 μm/cycle). After completing all the steps, the resulting photo-polymerized construct was thoroughly washed with acetone and vacuum-dried.

2.7. Microscopy observations

A photo-polymerized construct was observed under a scanning electron microscope (SEM, JSM-840A, JEOL Ltd., Tokyo, Japan) after sputter coating with gold. The histological analysis of the subcutis of a rat was carried out under a light microscope (Olympus VANOX-S AHBS, Tokyo, Japan).

2.8. Cell culture examination

A photo-polymerized construct or film was sterilized with 70% ethanol, washed with PBS, air-dried, and placed at the bottom of a 24-well culture dish (Corning, NY). Fibroblasts (Swiss3T3, obtained from American Type Culture Collection, 5×10^4 cells/well) were seeded into the dish with Dulbecco's modified Eagle's medium (DMEM, Life Technologies Inc., Rockville, MD) supplemented with 10% fetal bovine serum (FBS, Life Technologies). The cells were maintained at 37 °C in a

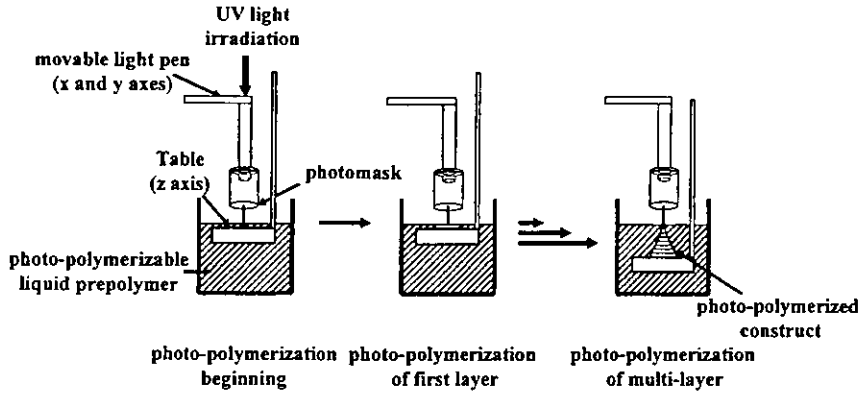

Fig. 2. Scheme of layer-by-layer photo-polymerization using a custom-designed microstereolithographic (μSL) rapid photo-typing apparatus.

humidified 5% CO_2 atmosphere. The cell number on the film was determined by NIH Image Software, and observation was carried out under a phase-contrast microscope (TE300, Nikon, Tokyo, Japan) after a certain incubation period.

2.9. *In vivo hydrolytic degradation behavior*

The photo-polymerized microcone array made of P(T/P200) or P(T/P1k) was washed with ethanol and vacuum-dried, then was implanted under the dorsal subcutis of a female Wister rat (about 400 g in weight). After 1- or 4-week implantation, the rat was dissected to remove the construct from the subcutis.

2.10. *Preparation of drug-loaded photo-polymerized constructs and implantation*

The microcone array, a photo-polymerized micro-architectural construct made of P(T/P200) or P(T/P1k), was immersed in 10 wt% dexamethasone (Sigma) aqueous solution for 2 days, washed with ethanol and vacuum-dried. The drug-loaded construct was implanted under the dorsal subcutis of a female Wister rat. After 1-week implantation, the rat was dissected to remove the surrounding tissue of the construct. The tissue was fixed in 1% aqueous formaldehyde solution (pH 7.4) for 12 h, and stained with hematoxylin eosin (HE).

3. Results

3.1. *Preparation of liquid acrylated TMC-based prepolymers and photo-polymerizing characteristics*

A series of liquid acrylated TMC-based prepolymers were prepared using a triol (TMP) or linear PEG with a molecular weight of 200 or 1000 [prepolymer codes were given as T/P200, T/P1k and T/TMP and their photo-polymerized films or constructs were designated as P(T/P200), P(T/P1k) and P(T/TMP), respectively, where T denotes TMC, and P200 and P1k denote PEG with molecular weights of 200 and 1000, respectively]. The TMP-based prepolymer is a trifunctional acrylated prepolymer, and the PEG-based prepolymers are bifunctional acrylated prepolymers. Table 1 summarizes the prepolymer compositions, degrees of acrylation, the molecular weights, and the viscosities of prepolymers. The resultant prepolymers (90–98% acrylation determined by ^{1}H-NMR spectroscopy) were viscous liquids. Viscosities of the prepolymers determined by a cone-and-plate viscometer ranged approximately 1.3–2.6 Pa s. The number-average molecular weights of the prepolymers, T/P200, T/P1k, and T/TMP, determined by GPC, were approximately 8×10^2, 2.4×10^3, and 1.1×10^3, respectively. The dependence of gel content of the network on UV-irradiation time for three acrylated prepolymers is shown in Fig. 3. Irrespective of the type of prepolymer, similar irradiation time-dependent photo-polymerizing characteristics of the prepolymers were observed: more than 95% of yield was achieved

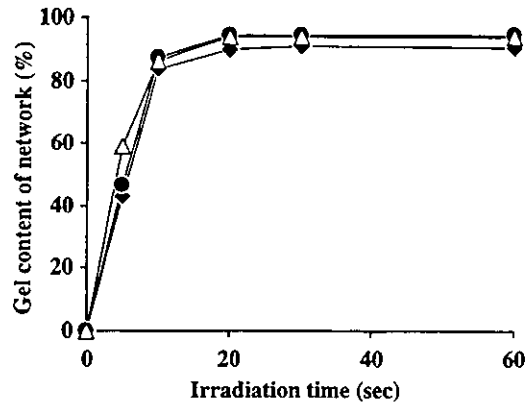

Fig. 3. UV-induced gel content of the network of TMC-based liquid prepolymers at an irradiation of 2 W/cm^2. Film thickness: 0.2 mm P(T/P200) (●), P(T/P1k) (♦), and P(T/TMP) (△).

within 20 s of photo-irradiation. Regarding the water contact angles of completely photo-polymerized films, PEG-based films exhibited low receding angles [27° for P(T/P200) and less than 5° for P(T/P1k)], whereas P(T/TMP) exhibited a relatively high receding angle (47.4°) (Table 1). Following the immersion of photo-polymerized films (photo-irradiation time; 1 min, photo-intensity; 2 W/cm^2) in water for 2 days, degree of water adsorptivity (DW) defined as Eq. (1) was as follows: approximately 30% for P(T/P1k), 2% for P(T/P200) and 1% for P(T/TMP) (Table 1).

3.2. *Microstereolithographically (μsl) photo-polymerized constructs*

Fig. 4 shows the design configurations of four different microarchitectural constructs (micropillar array, microcone array, microbank array on a platform plate, and multi-microtunnels on a glass plate). After the platform plates were prepared using a prepolymer, various microarchitectures were fabricated by layer-by-layer photo-polymerization using the same prepolymer used for platform plates except for multi-microtunnels. Before microarchitectural constructs were photo-polymerized, a platform plate, on which a construct was formed, was prepared by two cycles of parallel UV scanning (size, 5 mm × 5 mm; height, 400 μm) (Figs. 4A–C). Fig. 5A shows the micropillar array in which pillars (approximately 400 μm in diameter and 1200 μm in height) were formed on the platform plate, which was prepared by eight cycles of programmed scanning. Fig. 5B shows the microcone array (bottom diameter of cone, 650 μm; top diameter, 100 μm; height, 1800 μm) formed on the platform plate, which was photo-polymerized by gradually decreasing the diameter of the movable light pen from 500 to 0 μm (number of cycles of programmed scanning: 11). Fig. 5C shows the microbank array (width of bank, 300 μm; length, 5 mm; height, 1200 μm) formed on the platform plate (number of cycles: 8). Multi-microtunnels were prepared according to the configuration (Fig. 4D) on the glass plate at different cycles of layer photo-polymerization, and then stood up the constructs (see Fig. 6). The resultant constructs were easily removed from the glass plate.

Fig. 6 shows two types of multi-microtunnels; The first multi-microtunnel contains nine microtunnels

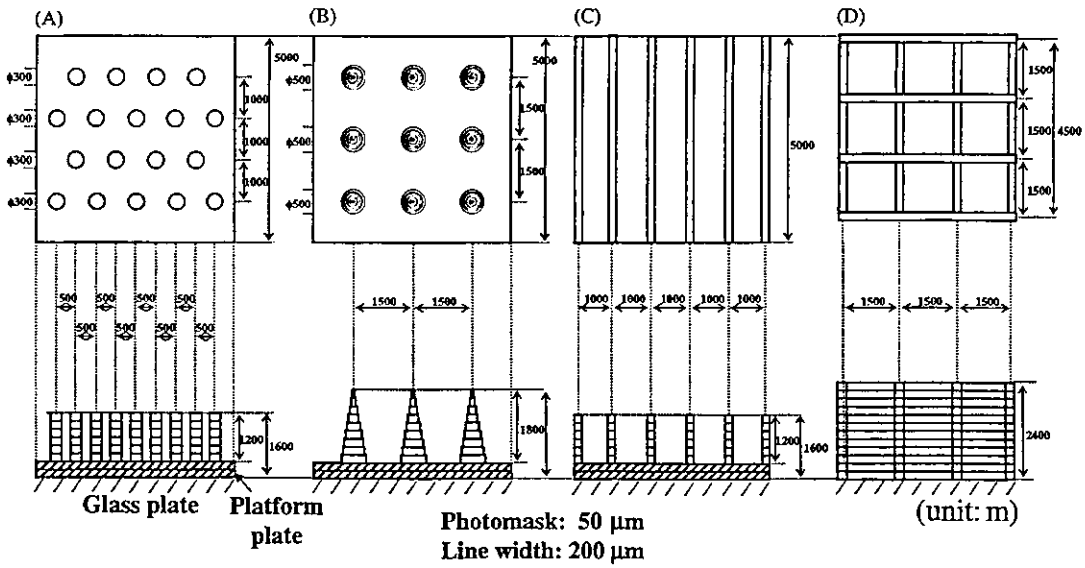

Fig. 4. Design configurations of microarchitectured constructs. Upper panels: top views; lower panel: cross-sectional views. (A) Micropillar array; (B) microcone array; (C) microbank array; and (D) multi-microtunnels.

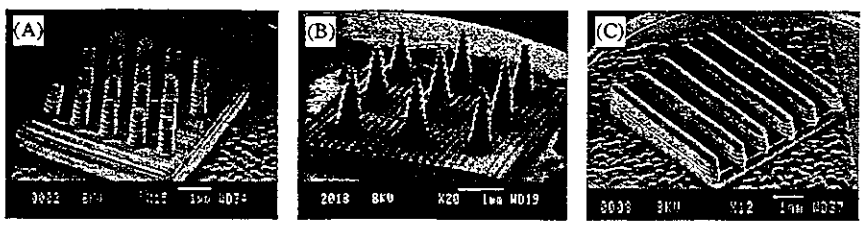

Fig. 5. SEM images of (A) micropillar array, (B) microcone array, and (C) microbank array prepared from the P(T/P200).

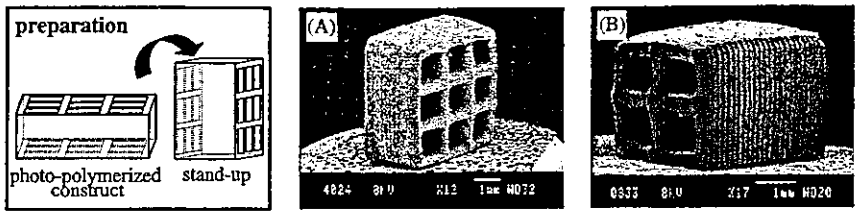

Fig. 6. SEM images of multi-microtunnels prepared from P(T/P200), (A) nine tunnels and (B) four tunnels.

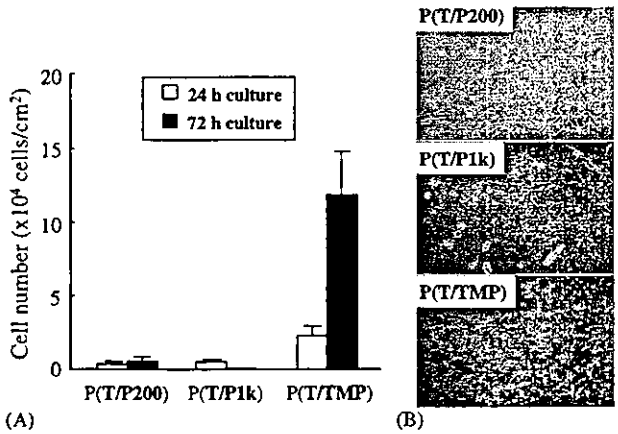

Fig. 7. Cell adhesion potential on three different photo-polymerized films: (A) cell number and (B) microscopy observation of the photo-polymerized films at 72 h culture.

(Fig. 6A). Each of the nine square microtunnels has a height and width of 800 μm and a tunnel length of 2400 μm (number of cycles: 12). Fig. 6B depicts four square microtunnels, each with a height and width of approximately 800 μm, and a tunnel length of 5000 μm (number of cycles: 25).

3.3. Cell adhesion potentials of photo-polymerized films

To determine the cell adhesion potential of photo-polymerized films, fibroblasts were seeded and cultured for up to 72 h. Both PEG-based films, P(T/P200) and P(T/P1k), exhibited a very low cell adhesion potential; concomitantly, markedly reduced spread and proliferation were observed. On the other hand, the relatively hydrophobic film (P(T/TMP)) exhibited a high cell adhesion and proliferation potentials as shown in Fig. 7.

3.4. Multi-microwells and composite microbank array for cell culture

Fig. 8 shows the multi-microwells prepared by photo-polymerization of noncell-adhesive P(T/P200) formed on the glass surface. Square wells were prepared by the photo-polymerization of cross-hatched banks (each well has the following dimensions: 800 μm × 800 μm, height of bank: about 200 μm) using a movable light pen for each 1 mm of square well (number of cycles: 1). When fibroblasts were seeded and cultured for 3 days on the multi-microwells, cells adhered and proliferated in the glass surface of wells, but little cell adhesion was observed on the banks. Fig. 9 shows the composite microbank array, which consisted of the plate with cell adhesive P(T/TMP) and microbanks with noncell-adhesive P(T/P200). Regarding the composite constructs, after completing the process using one liquid prepolymer, the construct, which was fixed on a *z*-axis movable table, was thoroughly washed with acetone and another liquid prepolymer bath was set at the depth of about 200 μm for the next photo-polymerization. Cells did not adhere to the banks, but cells well adhered and spread on the plate.

3.5. In vivo hydrolytic degradation behavior

Microcone arrays made of P(T/P200) and P(T/P1k) were implanted under the dorsal subcutis of a rat for 1 and 4 weeks. Fig. 10 shows the SEM images before and after the implantation. Some of the microcones in an array made of poorly swellable P(T/P200) were broken, probably due to tissue friction during implantation, and the crack size on the surface was slightly higher in 4-week implantation period (Figs. 10A, C, and E). On the other hand, for the microcone array made of highly swellable P(T/P1k), neither fracture nor cracks were observed for the swollen microarrays when harvested from tissues. However, SEM images showed large cracks, which were apparently created due to shrinkage during vacuum drying procedure for SEM sample preparation. The degree of crack formation at 4-week implantation appeared to be larger than that at 1-week implantation, suggesting that the degradation of P(T/P1k)-based photo-polymerized construct occurred not only on the surface but also in the bulk (Figs. 10B, D, and F).

3.6. Implantation of drug-loaded photo-polymerized constructs

An anti-inflammatory water-soluble drug (dexamethasone) in an aqueous solution was applied to two microcone arrays with different swelling properties;

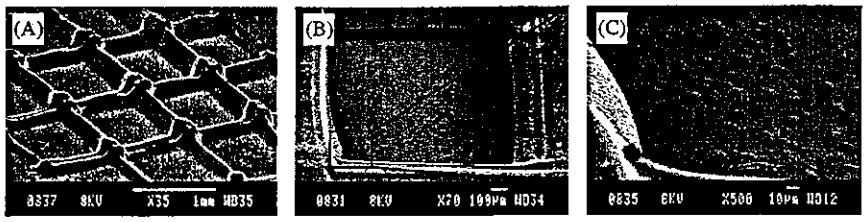

Fig. 8. SEM images of cell-seeded multi-microwells prepared from P(T/P200) on a glass surface: (A) multi-microwells and (B) and (C) microphotograph of a cell adhering only to the glass surface.

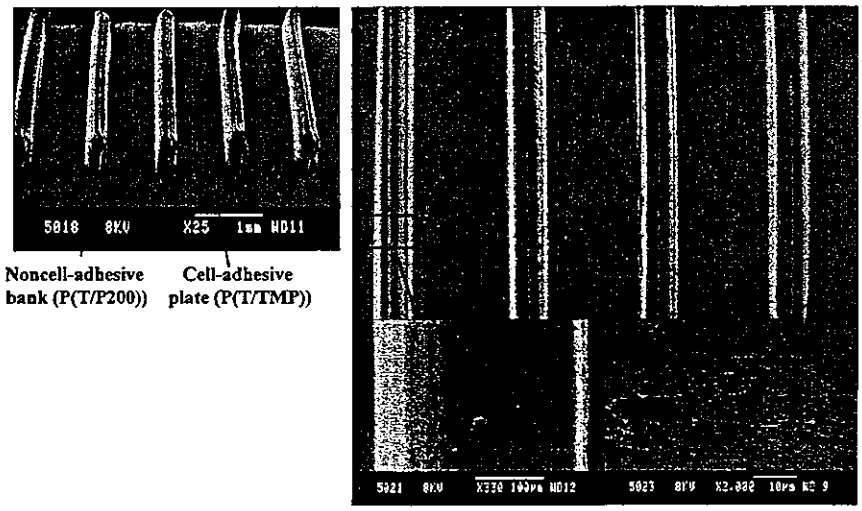

Fig. 9. SEM images of composite construct composed of a plate with cell-adhesive P(T/TMP) and microbanks with noncell-adhesive P(T/P200).

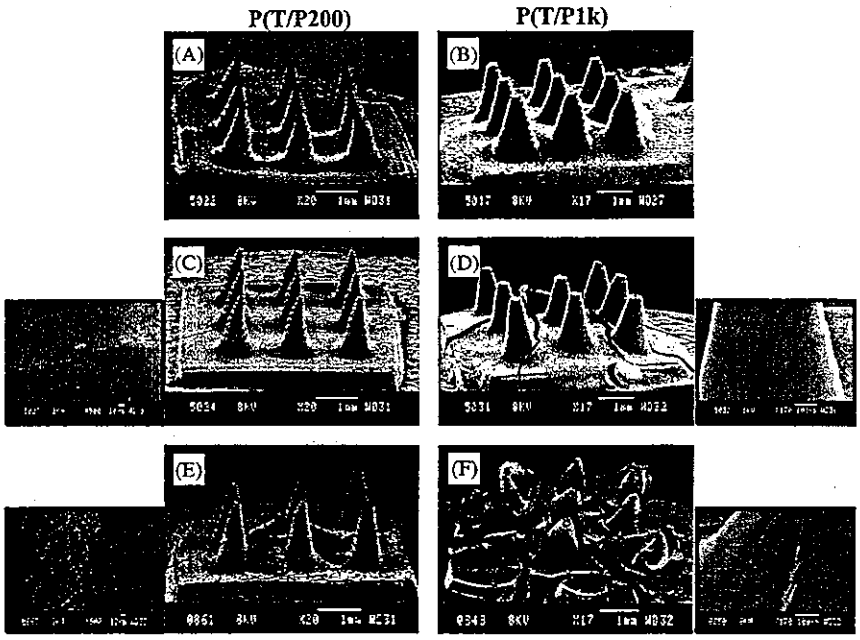

Fig. 10. SEM images of microcone array composed of P(T/P200) or P(T/P1k) implanted under the dorsal subcutis of a rat. Before implantation (A, B), at 1-week implantation (C, D) and at 4-week implantation (E, F).

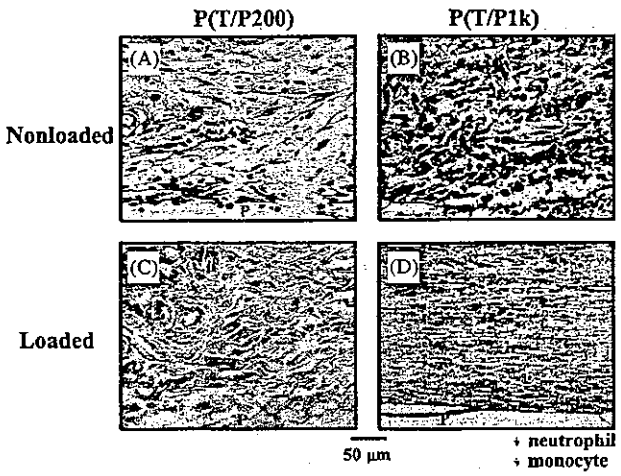

Fig. 11. Histological cross-sectional microphotographs of subcutaneous tissues surrounding the implanted photo-polymerized construct at 1-week implantation; nonloaded (A, B) and dexamethasone-loaded (C, D).

highly swellable P(T/P1k) and poorly swellable P(T/P200). The nonloaded or drug-loaded microcone arrays were implanted under the dorsal subcutis of rats and the surrounding tissues of implanted photo-polymerized constructs at 1-week implantation were harvested. Differences in the features of tissues surrounding the constructs between nonloaded and dexamethasone-loaded microcone arrays and also between P(T/P1k)- and P(T/P200)-derived microcone arrays were observed. A large number of fibroblasts and leucocytes, such as neutrophils and monocytes, induced due to the foreign-body antigenic inflammatory reaction invaded into the subcutis surrounding the nonleaded construct made of P(T/P1k) (Fig. 11B). The extent of foreign-body inflammatory reaction decreased in the order: nonloaded P(T/P1k)-based $\gg$ nonleaded P(T/P200)-based > drug-loaded P(T/P200)-based $\gg$ drug-loaded P(T/P1k)-based. Irrespective of the type of construct, drug-loading significantly reduced the invasion of cells into the surrounding tissues (Fig. 11). Such a tendency was more prominent for P(T/P1k) than for P(T/P200). Leucocytes were hardly observed in tissues surrounding the drug-loaded construct made of P(T/P1k) (Fig. 11D). This indicates that photo-polymerized construct made of drug-loaded P(T/P1k) minimized the inflammatory reaction.

4. Discussion

SL using the layer-by-layer photo-fabrication method, which employs computer-aided manufacturing (CAM), light beam, and photo-polymerizable prepolymers, allows the generation of complex 3D constructs [1-4]. Using the SL technique, various medical applications, such as photo-polymerized constructs of micro-architectural surfaces and precision micro- and macroshaped devices for drug delivery matrices, implants and scaffolds for engineered tissues may be feasible using biocompatible biodegradable photo-polymerizable liquid prepolymers with the ability to rapidly solidify upon UV irradiation, but only few applications have been utilized [10,17]. For biomedical applications, the design of photo-polymerizable biocompatible liquid prepolymers is essentially required. However, only a few studies on such prepolymers were reported. Along with the design criteria satisfying the requirements for biomedical applications, we prepared multi-functional liquid prepolymers based on TMC and CL, which were capped with an acrylate group at the ends, because both TMC and CL can be metabolized in the body. Cooke et al. has developed a 3D photo-polymerized bone substrate, the external surface and internal geometry of which was of the actual size for implantation (50 mm diameter and 4 mm thick), prepared from a biodegradable poly(propylene fumarate) (PPF) with a photo-initiator using a commercially available SLA device [17].

In our previous study, we synthesized biodegradable liquid acrylated TMC-based prepolymers, which were initiated by tri-ol (TMP) or linear PEGs with a mol. wt. of 200 or 1000, and then evaluated the photo-polymerizing characteristics and hydrolytic behavior after photo-polymerization by visible-light irradiation; the photo-polymerized films derived from a low molecular weight PEG (PEG200) and TMP exhibited a much lower hydrolysis potential than PEG1000-derived polymers in terms of weight loss, water uptake, swelling depth, and micromechanical properties of the surface [18].

In this article, precisely designed microarchitectures were photo-polymerized using the three different acrylated liquid prepolymers [T/P200, T/P1k, and T/TMP], which exhibited liquid-to-solid transformation within 10–20 s of UV-irradiation at a photo-intensity of 2 W/cm^2 at 365 nm, irrespective of prepolymer (Table 1 and Fig. 3). Our custom-designed μSL apparatus consisted of a movable light pen for the x and y axes with a photo-mask, a movable table for the z axis, UV-light source, and liquid prepolymer bath operated using the CAD/CAM system was useful for photo-polymerizing microscale constructs as evidenced in the SEM images, such as the micropillar array, microcone array, microbank array, and multi-microtunnels, which may have possible applications such as the microarchitectural surfaces for drug releasing or the cell platform for guidance and the 3D spatio-regiospecific segregation matrix for tissue engineering (Figs. 5 and 6).

Our results showed that PEG-based hydrophilic photo-polymerized films [P(T/P200) and P(T/P1k)],

whose receding contact angles were 27° and less than 5°, respectively, exhibited a very low cell adhesion potential, whereas P(T/TMP) (receding contact angle, 47.4°) exhibited high cell adhesion and proliferation potentials (Table 1 and Fig. 7). Exploiting these differences in properties between hydrophilic and relatively hydrophobic TMC-based prepolymers, functionally designed microarchitectural constructs such as multi-microwells with noncell adhesion potential (P(T/P200)) on the glass surface and composite microbank array which consisted of a cell-adhesive plate (P(T/TMP)) and noncell-adhesive banks (P(T/P200)) were photo-polymerized. Cells only adhered and spread inside the square wells (on the glass surface) in the multi-microwells (Figs. 8B and C). Well-adhered and spread cells were observed on the plate for composite microbank array, whereas cells were hardly observed on the PEG-based prepolymer-derived banks (Fig. 9). Regarding drug-releasing micro-architectured surfaces, implanted microcone arrays impregnated with or without an anti-inflammatory drug, dexamethasone, affected the polymer-dependent degree of foreign-body inflammatory reactions, which induced neutrophils, monocytes, lymphocytes, and fibroblasts. The degree of reaction was decreased in the order: nonloaded P(T/P1k)-based $\gg$ nonloaded P(T/P200)-based $>$ drug-loaded P(T/P200)-based $\gg$ drug-loaded P(T/P1k)-based (Fig. 11). This tendency is probably due to the different hydrolytic characteristics of the two polymers such as degree of water adsorptivity (2% for P(T/P200) and 30% for P(T/P1k), respectively) and degradation rate in vivo (Table 1 and Fig. 10). That is, a highly swellable and fast degradable P(T/P1k)-based photo-polymerized construct can take up and release a large amount of an aqueous drug solution than a poorly swellable and slow degradable P(T/P200)-based construct.

5. Conclusion

In this study, precisely and functionally designed microarchitectural constructs made of photo-polymerizable biodegradable TMC-based liquid prepolymers have been photo-polymerized using a custom-designed μSL apparatus automated by CAD system. The μSL-driven photo-polymerized construct having a wide scope of hydrolytic characteristics and cell adhesive/noncell adhesive properties can provide advanced precision microfabricated devices for drug delivery matrices, implants and engineered tissues. Our next target using μSL with these liquid prepolymers is to fabricate a few tenths micron-order microneedle-array-covered stent to minimize excessive tissue ingrowth (intimal hyperplasia) in atherosclerotic vessels, which will be realized using a μSL two-photon system.

Acknowledgements

The authors thank Dr. S. Imayama (MD), Department of Dermatology, Kyushu National Hospital, for the histological analysis and Dr. T. Kanemaru of the Faculty of Medicine, Kyushu University, for SEM. This study was financially supported in part by a Grant-in-Aid for Scientific Research (A2-15200038) from MEXT, Japan.

References

[1] Kodama H. Automatic method for fabricating a three-dimensional plastic model with photohardening polymer. Rev Sci Instrum 1981;52:770–3.
[2] Herbert AJ. Solid object generation. J Appl. Photographic Eng 1982;8:185–8.
[3] Yakunin VP. Laser stereolithography as a wasteless technology for rapid layer by layer production of parts from liquid polymers. Liteinoe Proizvodstvo 1999;7:5–6.
[4] Kulkarni RB, Manners CR. Stereolithographic process of making a threedimensional object. US Patent No. 6,558,606, 2003.
[5] Eufinger H, Wehmoller M, Machtens E, Heuser L, Harders A, Kruse D. Reconstruction of craniofacial bone defects with individual alloplastic implants based on CAD/CAM-manipulated CT data. J Craniomaxillofac Surg 1995;23:175–81.
[6] Eufinger H, Pack M, Terheyden H, Wehmoller M. Experimental computer-assisted alloplastic sandwich augmentation of the atrophic mandible. J Oral Maxillofac Surg 1999;57:1436–41.
[7] Poulsen M, Lindsay C, Sullivan T, D'Urso P. Stereolithographic modeling as an aid to orbital brachytherapy. Int J Radiat Oncol Biol Phys 1999;44:731–5.
[8] Binder TM, Moertl D, Mundigler G, Rehak G, Franke M, Delle-Karth G, Mohl W, Baumgartner H, Maurer G. Stereolithographic biomodeling to create tangible hard copies of cardiac structures from echocardiographic data: *in vitro* and *in vivo* validation. J Am Coll Cardiol 2000;35:230–7.
[9] Hutmacher D. Scaffold design and fabrication techniques for engineering tissues-state of the art future perspectives. J Biomater Sci Polym Edn 2001;12:107–24.
[10] Cooke MN, Fisher JP, Dean D, Rimnac C, Mikos AG. Use of stereolithography to manufacture critical-sized 3D biodegradable scaffolds for bone ingrowth. J Biomed Mater Res 2002;64B:65–9.
[11] Matsuda T, Mizutani M, Arnold SC. Molecular design of photocurable liquid biodegradable copolymers. 1. Synthesis and photocuring characteristics. Macromolecules 2000;33:795–800.
[12] Matsuda T, Mizutani M. Molecular design of photocurable liquid biodegradable copolymers. 2. Synthesis of coumarin-derivatized oligo(methacrylate)s and photocuring. Macromolecules 2000;33:791–4.
[13] Mizutani M, Matsuda T. Photocurable liquid biodegradable copolymers: *in vitro* hydrolytic degradation behaviors of photocured films of coumarin-end-capped poly(ε-caprolactone-co-trimethylene carbonate). Biomacromolecules 2002;3:249–55.
[14] Mizutani M, Matsuda T. Liquid photocurable biodegradable copolymers: *in vivo* degradation of photocured poly(ε-caprolactone-co-trimethylene carbonate). J Biomed Mater Res 2002;61:53–60.
[15] Mizutani M, Arnold SC, Matsuda T. Liquid phenylazide-end-capped copolymers of ε-caprolactone and trimethylene carbonate: preparation, photocuring characteristics and surface layering. Biomacromolecules 2002;3:668–75.

[16] Matsuda T, Mizutani M. Liquid acrylate-end-capped biodegradable poly (ε-caprolactone-co-trimethylene carbonate). I. Preparation and visible light-induced photocuring characteristics. J Biomed Mater Res 2002;62:387–94.
[17] Mizutani M, Matsuda T. Liquid acrylate-end-capped biodegradable poly (ε-caprolactone-co-trimethylene carbonate). II. Computer-aided stereolithographic microarchitectural surface photoconstructs. J Biomed Mater Res 2002;62:395–403.
[18] Matsuda T, Kwon IK, Kidoaki S. Photocurable biodegradable liquid copolymers: synthesis of acrylate-end-capped trimethylene carbonate-based prepolymers, photocuring and hydrolysis. Biomacromolecules 2004;5:295–305.

Available online at www.sciencedirect.com
SCIENCE DIRECT®
Biomaterials 26 (2005) 3105–3111
Biomaterials
www.elsevier.com/locate/biomaterials

Poly(*N*-isopropylacrylamide) (PNIPAM)-grafted gelatin hydrogel surfaces: interrelationship between microscopic structure and mechanical property of surface regions and cell adhesiveness

Shoji Ohya[a,*], Satoru Kidoaki[b], Takehisa Matsuda[b]

[a]*Department of Bioengineering, National Cardiovascular Center Research Institute, 5-7-1 Fujishirodai, Suita, Osaka 565-8565, Japan*
[b]*Division of Biomedical Engineering, Graduate School of Medicine, Kyushu University, 3-1-1 Maidashi Higashi-ku, Fukuoka 812-8582, Japan*

Received 24 May 2004; accepted 23 August 2004
Available online 30 September 2004

Abstract

Poly(*N*-isopropylacrylamide)-grafted gelatin (PNIPAM-gelatin) serves as a temperature-induced scaffold at physiological temperature. This study was aimed at determining the effect of the graft architecture of thermoresponsive PNIPAM-gelatin on the surface topography and elastic modulus of the hydrogels prepared with different architectured PNIPAM-gelatins: the surface topography and elastic modulus were determined by atomic force microscopy (AFM). PNIPAM-gelatin surfaces showed an irregularly concavo-convex structure with a vertical interval of approximately 1 μm regardless of the weight ratio of PNIPAM to gelatin (P/G: 5.8, 12, and 18). The elastic moduli of hydrogels varied at measured sites. The mean elastic moduli of PNIPAM-gelatin with the lowest P/G were low, but increased with increasing P/G. Human umbilical vein endothelial cells adhered and spread on PNIPAM-gelatin hydrogels with the highest P/G, whereas reduced adhesion and nonspreading, round-shaped cells resided on the hydrogels with lower P/Gs. Interrelationship between elastic modulus and cell adhesion and spreading potentials were discussed from physicochemical and cellular biomechanical viewpoints.

Keywords: Poly(*N*-isopropylacrylamide)-grafted gelatin; Atomic force microscopy; Microscopic structure; Mechanical property; Cell adhesiveness

1. Introduction

Tissue engineering has recently been proposed as a promising therapeutic discipline for repairing or to replace diseased or lost tissues; moreover, some engineered tissues have been used for clinical applications [1–4]. Such tissues are fabricated ex vivo or in vivo with or without using synthetic or biologically derived macromolecules so as to provide an appropriate extracellular milieu. To reconstruct a functional tissue, the micro-extracellular environment for incorporated cells is essential. The extracellular space should be incorporated with a cell adhesion matrix and/or structural platform, and interconnected (microscopic) voids in order to facilitate a supply of oxygen and nutrients to cells, cell migration and tissue ingrowth.

We recently prepared a thermoresponsive artificial extracellular matrix (ECM), poly(*N*-isopropylacrylamide)-grafted gelatin (PNIPAM-gelatin) [5–8], which is prepared by quasi-living radical graft polymerization initiated from a gelatin molecule [9,10], and evaluated how the viability and proliferation of cells entrapped in a three-dimensional (3D) hydrogel depended on the graft architecture, including graft chain density and graft chain length of PNIPAM-gelatin [8]. As a rough approximation, bovine smooth muscle cells proliferated well in hydrogels prepared using PNIPAM-gelatin with a high weight ratio of PNIPAM to gelatin (P/G).

In this study, we investigated how cell adhesion on a hydrogel surface is influenced by the graft architecture

*Corresponding author. Tel.: +81-6-6833-5012; fax: +81-6-6872-8090.
E-mail address: ohya@ri.ncvc.go.jp (S. Ohya).

0142-9612/$ - see front matter © 2004 Elsevier Ltd. All rights reserved.
doi:10.1016/j.biomaterials.2004.08.006

of PNIPAM-gelatin. The effects of surface topography and surface mechanical strength, both of which are determined by atomic force microscopy (AFM), on cell adhesion and spreading potentials were evaluated and discussed from the physicochemical and biomechanical viewpoint.

2. Materials and methods

2.1. Materials

1-Ethyl-3-(3-dimethylaminopropyl) carbodiimide hydrochloride (WSC) was obtained from Dojindo Laboratories (Kumamoto, Japan). *N*-isopropylacrylamide (NIPAM) and 4-chloromethyl benzoic acid were obtained from Tokyo Chemical Industry Ltd. (Tokyo, Japan). NIPAM was used after recrystallization using a toluene–hexane solution. Gelatin (molecular weight: approximately 9.5×10^4 g/mol, from bovine bone) and sodium *N*,*N*-diethyldithiocarbamate trihydrate were obtained from Wako Pure Chemical Industry Ltd. (Osaka, Japan). Solvents and other reagents, all of which are of reagent grade, were purchased from Wako and used after conventional purification.

2.2. Preparation of PNIPAM-gelatin hydrogel

PNIPAM-gelatins with different graft densities (approximately 11, 23, and 34 graft chains per gelatin molecule; average molecular weight of the graft chain: approximately 5.0×10^4 g/mol) were prepared according to the procedure described previously [5–8]. Briefly, the amino groups of gelatin were reacted with the carboxyl group of 4-dithiocarbamylmethyl benzoic acid using the condensation reagent, WSC. The degree of dithiocarbamylation was adjusted with reaction time. Subsequently, NIPAM was polymerized from dithiocarbamate-derivatized gelatin in water under UV irradiation for 10 min (400 W Hg lamp, AH400RP, UV, Saitama, Japan; light intensity at 250 nm: 4.0 mW/cm^2). By graft density, three different PNIPAM-gelatins were prepared (PNIPAM/gelatin weight ratios (P/G) = 5.8, 12, and 18). Hydrogels were prepared from PNIPAM-gelatins with different P/G at 5 and 20 w/v% of aqueous solution. (Chemical structures are shown in Fig. 1). The aqueous or M199 solutions of PNIPAM-gelatins (concentration: 5 and 20 w/v%, 100 μL) placed on the tissue culture dish (diameter: 35 mm, Iwaki Glass, Tokyo, Japan) fixed on the stage of AFM equipment were warmed to 37 °C to form white opaque hydrogels. The water or M199 was added onto the hydrogel, which were subjected to surface topological and mechanical strength characterizations described below. The formed hydrogel tightly adhered on the bottom of the dish.

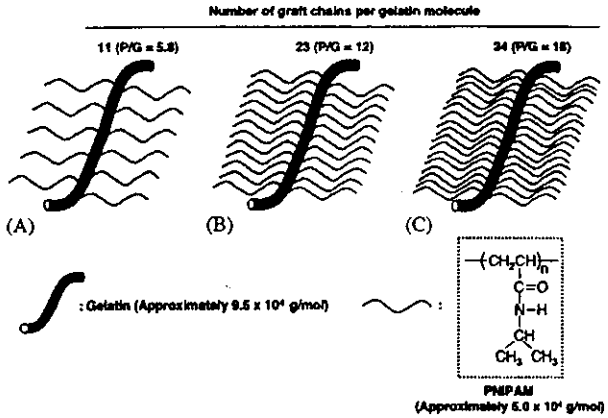

Fig. 1. Schematic structure of PNIPAM-gelatins with different graft chain densities.

2.3. Surface observation and elastic modulus

The surface images and force-versus-indentation (F–δ) curves of the hydrogels in water or M199 at 37 °C were measured by AFM (Nanoscope IIIa, Dimension 3000, Digital Instruments), using a commercial Si_3N_4 probe tip (manufacturing spring constant: 0.06 N/m (the value was used for the calculation of elastic modulus without further validation. Since the same tip was used throughout the study, the discussion was made on basis of the relative values); Digital Instruments, Santa Barbara, CA, USA). The probe tip was equipped with a commercial fluid cantilever folder (Digital Instruments), and immediately immersed into water or M199. The measurement was performed in water or M199 at 37 °C. To control sample temperature, AFM equipment was placed in a box maintained at 37 °C using heater with a thermocontroler (Nikon, Japan). Surface images (Scanning size: 10 μm × 10 μm) were obtained by a tapping mode (resonance frequency: 7.0 kHz).

F–δ curves were measured linearly every 100 nm (total of 101 points measured) by a contact mode. Elastic moduli were calculated from the F–δ curves according to the Hertz model described below [11]. If the tip is infinitely stiff and conical in shape, the Hertz model predicts

$$F = \frac{2\tan\alpha}{\pi}\frac{E}{1-\upsilon^2}\delta^2, \tag{1}$$

where F is the loading force, E is the elastic modulus, υ is the Poisson ratio, α is the open angle of the tip, and δ is the indentation depth. Here, open angle α was 35° and Poisson ratio υ was fixed to 0.5 for simplification. Therefore, elastic moduli were calculated from F–δ curves fitted to the equation using a linear least-squares method.

2.4. Cell adhesiveness on PNIPAM-gelatin hydrogels

Human umbilical vein endothelial cells (HUVECs) were stained with a fluorescent dye of benzoxazolium, 3-octadecyl-2-[3-(3-octadecyl-2(3H)-benzoxazolylidene)-1-propenyl]-, perchlorate (DiO, Molecular Probes Inc., Eugene, USA), before use. M199 solutions (70 μL) of PNIPAM-gelatin (P/G = 5.8, 12, and 18, concentration; 5 w/v% or 20 w/v%) were placed on the surface enclosed with a stainless-steel ring ($\varnothing = 15$ mm) placed in the tissue culture dish at room temperature. The dish was placed in humidified 5% CO_2 incubator for 30 min to form a white opaque hydrogel. An M199 (10% FCS, 0.5 mL) suspension of HUVECs (cell density: 2.0×10^4 cells/mL) was poured onto the hydrogel maintained at 37 °C. After 2 days of incubation, cell morphology was observed by confocal laser scanning microscopy (Radiance 2000, Biorad, CA, USA) (wavelength: 488 nm (excitation) and 510 nm (fluorescence)).

3. Results

Hydrogels were prepared by thermal phase inversion using three PNIPAM-gelatins with different graft chain densities (Figs. 1A–C). These PNIPAM-gelatins have approximately 11, 23, and 34 graft chains per gelatin molecule but have a fixed average molecular weight of the graft chain (approximately 5.0×10^4 g/mol). The weight ratios (P/G) of the grafted chain (PNIPAM) to the main chain (gelatin) of these three PNIPAM-gelatins were 5.8, 12, and 18 in accordance with the graft chain density. The concentrations of PNIPAM-gelatins in hydrogels thus prepared were 5 and 20 w/v% of water and M199 culture medium. These hydrogels were adhered on the bottom of the dishes. Surface topography and surface micro-mechanical strength were determined by AFM. Cell adhesion and spreading of fluorescently labeled HUVECs on these hydrogel surfaces were determined by confocal laser scanning microscopy.

3.1. Microscopic topography of hydrogels

AFM images obtained in water or M199 show that all the surfaces of PNIPAM-gelatin hydrogels have microscopic concavo-convex structure as clearly injected by scattered dark or bright images, which may contain micropores and pits, regardless of P/G, PNIPAM-gelatin concentration, or solution (Fig. 2: upper). Fig. 2 (lower) shows the surface topographic images of these hydrogels of transversely scanned 10-μm-wide regions (dotted line in the upper figure). Increasing P/G appears to result in a more roughened topography with finer tiny pits (Figs. 2A–C). Several tiny pits with a depth of approximately half micrometer appeared in the scanned width of 10 μm. Little significant topographic difference was observed between those in water and in M199 (Figs. 2C and D). Reducing the concentration from 20 to 5 w/v% resulted in the disappearance of the tiny pits (Fig. 2E).

3.2. Elastic modulus of hydrogels

The micromechanical properties of more than 100 surface regions for each sample were determined by the force indentation (F–δ) technique. All the F–δ curves determined from the hydrogel surfaces along the dotted lines shown in Fig. 2 (upper) by the indentation of an AFM probe tip were parabolic (Fig. 3). Since a linear

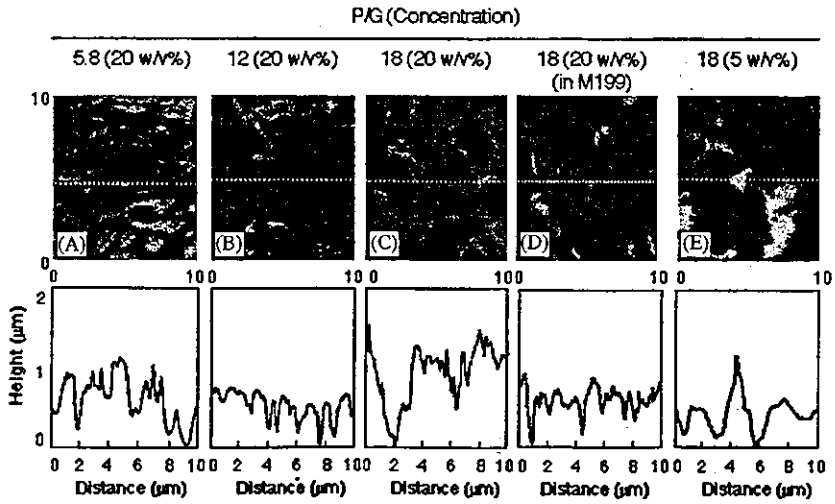

Fig. 2. Microscopic observation of PNIPAM-gelatin hydrogel surface by AFM in water (A)(B)(C)(E) and in M199 (D). Weight ratio of PNIPAM to gelatin (P/G): 5.8 for (A), 12 for (B), 18 for (C), (D) and (E). Hydrogel concentration: 20 w/v% for (A)(B)(C)(D), 5 w/v% for (E). Dark and bright areas are concave and convex areas, respectively.

relationship between F and δ^2 is held (Fig. 3B), the conical Hertz model was applied to calculate elastic moduli. Fig. 4 shows the relationship between the calculated elastic modulus and the height of the measured point for three hydrogels prepared at 20 w/v%, which was obtained from 101 points on each white-dotted line in Fig. 2 (the height is defined as the distance from the lowest or bottom line in the topography shown in Fig. 2: lower). The general tendency is that the elastic moduli appear to increase with increasing P/G, although the values of the determined elastic moduli were scattered. A majority of the elastic moduli of hydrogels with PNIPAM-gelatins of P/G of 5.8 were below 100 kPa, the average elastic modulus was 53 ± 21 kPa, and the height was less than 1 μm (Table 1 and Fig. 4). For hydrogels with PNIPAM-gelatin of P/G of 12, the population of elastic moduli higher than 100 kPa (around 20%) was increased. For hydrogels with P/G of 18, most of the moduli (more than 80%) were over 100 kPa irrespective of solutions. The average elastic moduli in water and M199 were 222 ± 64 and 244 ± 89 kPa, respectively. There is little significant difference in surface mechanical strength between hydrogels in water and in M199. These results indicate that highly aggregated PNIPAM were distributed on the hydrogel surface made of PNIPAM-gelatin with a high P/G of 18. At lower concentration (5 w/v%), the population of elastic moduli higher than 150 kPa decreased to 5% of the total population (data not shown). These indicate that a higher P/G and higher concentration result in a higher degree of aggregation and a higher surface distribution.

It is interesting to see how the elastic modulus of the hydrogel correlates with the surface topography (height). The calculated correlation coefficients are shown in Table 1. The correlation coefficients between surface topography and elastic modulus on PNIPAM-gelatin hydrogels with the lowest P/G of 5.8 were 0.3, whereas that of hydrogel with P/G of 18 was 0.45, implying that convex sites are stiffer than concave sites.

3.3. Cell adhesiveness on hydrogels

Confocal laser scanning microscopic images demonstrated the adhesion and spreading states of fluorescently labeled HUVECs on PNIPAM-gelatin hydrogels after two days of incubation (Fig. 5). Cells adhered and spread on hydrogels with higher P/Gs (12 and 18), but few cells adhered on that with P/G of 5.8. The number of spreading cells qualitatively appeared to increase with increasing P/G. At P/G of 18, there is a small difference between the spreading states of cells in 5 w/v% and 20 w/v% hydrogels.

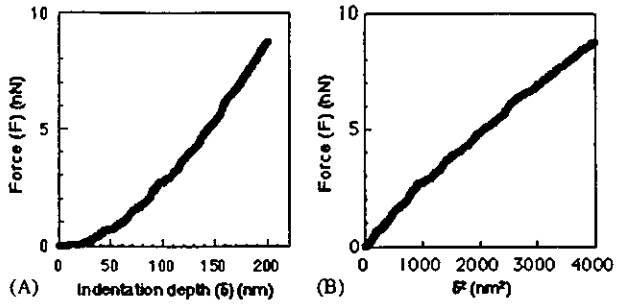

Fig. 3. (A) Force–indentation curve (F–δ curve) on PNIPAM-gelatin hydrogel by AFM. (B) F–δ^2 plots for analysis with Hertz model. Linear F–δ^2 using conical tip assumption.

4. Discussion

Cell adhesion, spreading and proliferation proceed via multiparameter-driven processes. Apart from biological factors (such as adhesion proteins and growth factors) and external mechanical-stress field (hydrodynamic and compressive forces), the substrate is a major determinant, which involves chemical compositions, mechanical properties and topography at the outer-surface region of the substrate. Almost three decades ago, Maroudas hypothesized that the rigidity or stiffness of the

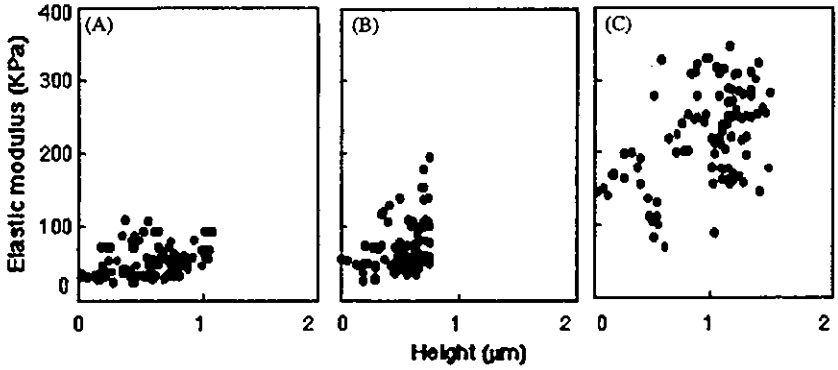

Fig. 4. Interrelationship between surface topography and elastic modulus evaluated from F–δ curves. The weight ratio of PNIPAM to gelatin (P/G): 5.8 for (A), 12 for (B), 18 for (C). Concentration (20 w/v%).

Table 1
Physical properties of PNIPAM-gelatin hydrogel

Hydrogel no.	PNIPAM-gelatin		Concentration (w/v%) (solution)	Elastic modulus (kPa)	Correlation coefficient[c]
	Graft density[a]	P/G[b]			
1	11	5.8	20 (water)	53±21	0.30
2	23	12	20 (water)	70±34	0.34
3	34	18	20 (water)	222±64	0.45
4	34	18	20 (M199)	244±89	ND[d]
5	34	18	5 (water)	52±36	ND[d]

[a]Number of graft chains per gelatin molecule.
[b]Weight ratio of PNIPAM to gelatin.
[c]Correlation coefficient between surface height and elastic modulus. Molecular weight of graft chain; approximately 5.0×10^4 g/mol (determined by GPC using PEG standards).
[d]ND; not determined. Number of measured points for each run were 101.

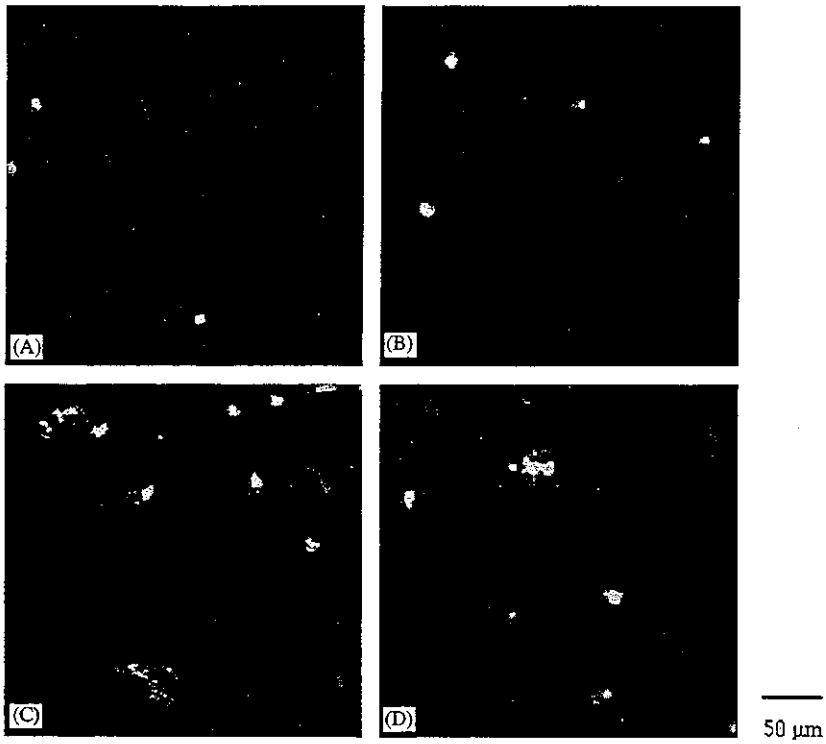

Fig. 5. Confocal laser scanning microscopic observation of HUVECs on PNIPAM-gelatin hydrogels. P/G: 5.8 for (A), 12 for (B), 18 for (C) and (D). Hydrogel concentration: 20 w/v% for (A)(B)(C), 5 w/v% for (D). HUVECs adhered and spread on hydrogels with P/G of more than 12. Cell morphology was dependent on P/G, not on the concentration of PNIPAM-gelatin.

substrate surface determines cell adhesiveness and the state of spreading. Such cell adhesiveness and spreading are enhanced by the rigidity of the substrate. Maroudas also postulated that cells require a rigid scaffolding to withstand tension exerted by spreading [12]. Using a deformable silicone thin film, Harris et al. showed that cell adhesion/spreading is strongly governed by surface rigidity/deformability [13]. Recently, Pelham and Wang demonstrated that cell focal adhesion and locomotion on flexibility-varied acrylamide gels are regulated by hydrogel substrate flexibility [14] and suggested the possible involvement of tyrosine phosphorylation, which is activated by local tension at adhesion sites [15,16]. Thus, many studies have implicated that mechanotransduction across the adhesion site between cell focal adhesion plaques and the extracellular matrix attached to the substrate determines cellular fundamental behaviors including adhesion, spreading, migration, proliferation, differentiation, re-differentiation, metastasis, and apoptosis.

The extracellular space design, which determines biological conditions suitable for cellular activities, is one of the most important factors in the fabrication of functional vital engineered tissues. Various design criteria have to be considered from the microscopic to the macroscopic level. The microenvironment on the hydrogel must determine the cell adhesiveness. In this study, we attempted to define the interrelationship between the microscopic surface structural and mechanical properties and cell adhesiveness of PNIPAM-gelatin hydrogel surfaces. Hydrogel surfaces, prepared by warming PNIPAM-gelatin aqueous and M199 solutions at 37 °C, were observed by AFM. All surfaces of PNIPAM-gelatin hydrogels have a nano-ordered concavo-convex structure over the scanning area, regardless of P/G (Fig. 2). The general tendency was that the hydrogel prepared using PNIPAM-gelatin with the highest P/G exhibited the most roughened surface topography (Fig. 2: C). It is suggested that the hydrogel contains interconnected micropores or voids, through which nutrients and oxygen can diffuse into the interior of the hydrogel.

On the other hand, the relationship between force (F) and indentation depth (δ) on the hydrogels fitted well to the conical Hertz model (linear relationship between F and δ^2; Fig. 3B) by which the elastic modulus was calculated. To validate how the measured elastic modulus is correct, we determined the elastic modulus (70 ± 11 kPa) of an agarose gel (3 w/v%) as standard sample. The obtained value reasonably agrees with the previously reported elastic modulus of 90 kPa [17,18]. As shown in Fig. 4, the calculated elastic moduli of PNIPAM-gelatin hydrogels increased with increasing P/G, although the measured values were scattered. It is speculated that the hydrogels must consist of roughly two domains in the continuous phase of water: One domain is a highly hydrated gelatin (soft) domain and the other is an aggregated PNIPAM (rigid) domain, which were formed by the intra- and inter-molecular associations of dehydrated PNIPAM graft chains, respectively. Our recent study showed that confocal laser scanning microscopic observation with reflection mode clearly demonstrated that hydrophobically clustered PNIPAM were scattered in the interior of the hydrogel [8]. For the hydrogel with P/G of 5.8, the major measured values were low, suggesting that the measured sites are associated with small-sized loosely aggregated PNIPAM domains. With an increase in P/G to more than 12, the obtained values became larger, indicating that the measured sites are associated with larger-sized, highly aggregated domains, the population and size of which must be increased with an increase in P/G.

The fine-structure and physical properties of hydrogel may change between water and culture medium due to containing many compounds such as salts and amino acids in culture medium. To examine the effect of the conditions, surface microtopography and elastic modulus measurement of hydrogel with P/G of 18 were conducted in cell culture medium of M199. The topography and elastic modulus were found to be similar to those in water (Table 1).

On the other hand, the correlation coefficients between the heights and elastic moduli of hydrogel surfaces were positive but not large (Table 1). However, an increased correlation coefficient with an increase in P/G was observed. Taken together with these lines of experimental evidence, it can be considered that most of convex region must be rigid, and concavo region must be soft (Fig. 4).

Cell adhesiveness was enhanced by increasing P/G (Fig. 5). A high P/G caused strong aggregation among PNIPAM chains, so that the higher strength of the hydrogel results in an enhanced higher capability of withstanding cell traction force, resulting in cell spreading. Thus, an appropriate balance of surface micromechanical strength derived from dehydrated PNIPAM aggregates and water-swollen cell-adhesive gelatin molecule provides cell adhesive and spreading environment on hydrogels. Scattered stiff regions probably derived from hydrophobically clustered PNIPAM may act as cell adhesion anchors which withstand against the cell traction strength.

5. Conclusion

Thermoresponsive hydrogels prepared using PNIPAM-gelatins with different architecture exhibited surfaces with concavo-convex structure, roughened surface topography and variable elastic modulus, both of which were determined by AFM. HUVECs adhered and spread well on the hydrogel prepared using PNIPAM-gelatin with a high P/G. These results show that surface elastic modulus can be a determinant of cellular behavior on hydrogels.

Acknowledgement

This study was financially supported by Ministry of Education, Culture, Sports, Science and Technology under Grant No. 14780665 and No. 15200038. One of the authors (S.O.) appreciates Dr. Y. Nakayama for technical advises.

Reference

[1] Bell E. Strategy for the selection of scaffolds for tissue engineering. Tissue Engineering 1995;1:163–79.
[2] Hutmacher DW, Goh JC, Teoh SH. An introduction to biodegradable materials for tissue engineering applications. Ann Acad Med Singapore 2001;30:183–91.

[3] Drury JL, Mooney DJ. Hydrogels for tissue engineering: scaffold design variables and applications. Biomaterials 2003;24:4337–51.
[4] Freed LE, Vunjak-Novakovic G, Biron RJ, Eagles DB, Lesnoy DC, Barlow SK, Langer R. Biodegradable polymer scaffolds for tissue engineering. Bio/Technology 1994;12:689–93.
[5] Morikawa N, Matsuda T. Thermoresponsive artificial extracellular matrix: *N*-isopropylacrylamide-graft-copolymerized gelatin. J Biomater Sci Polym Ed 2002;13:167–83.
[6] Matsuda T. Molecular design of functional artificial extracellular matrix: thermoresponsive gelatin. Jpn J Artif Organs 1999; 28:242–5.
[7] Ohya S, Nakayama Y, Matsuda T. Material design for artificial extracellular matrix: cell entrapment in poly(*N*-isopropylacrylamide) (PNIPAM)-grafted gelatin hydrogel. J Artif Organs 2001;4:308–14.
[8] Ohya S, Matsuda T. Poly(*N*-isopropylacrylamide) (PNIPAM)-grafted gelatin as thermoresponsive three-dimensional artificial extracellular matrix: molecular and formulation parameters vs. cell proliferation potential. Submitted for publication.
[9] Otsu T, Yoshida M, Tazaki T. A model for living radical polymerization. Makromol Chem Rapid Commun 1982;3:133–40.
[10] Nakayama Y, Matsuda T. Surface macromolecular architectural designs using photo-graft copolymerization based on photochemistry of benzyl *N,N*-diethyldithiocarbamate. Macromolecules 1996;29:8622–30.
[11] Weisenhorn AL, Khorsandi M, Kasas S, Gotzos V, Butt HJ. Deformation and height anomaly of soft surfaces studied with an AFM. Nanotechnology 1993;4:106–13.
[12] Maroudas NG. Chemical and mechanical requirements for fibroblast adhesion. Nature 1973;244:363–4.
[13] Harris AK, Wild P, Stopak D. Silicone rubber substrata: a new wrinkle in the study of cell locomotion. Science 1980;208:177–9.
[14] Pelham RJ, Wang YL. Cell locomotion and focal adhesions are regulated by substrate flexibility. Proc Natl Acad Sci USA 1997;94:13661–5.
[15] Zamir E, Katz M, Posen Y, Erez N, Yamada KM, Katz BZ, Lin S, Lin DC, Bershadsky A, Kam Z, Geiger B. Dynamics and segregation of cell-matrix adhesions in cultured fibroblasts. Nat Cell Biol 2000;2:191–6.
[16] Katz BZ, Zamir E, Bershadsky A, Kam Z, Yamada KM, Geiger B. Physical state of the extracellular matrix regulates the structure and molecular composition of cell-matrix adhesions. Mol Biol Cell 2000;11:1047–60.
[17] Nitta T, Haga H, Kawabata K, Abe K, Sambongi T. Comparing microscopic with macroscopic elastic properties of polymer gel. Ultramicroscopy 2000;82:223–6.
[18] Haga H, Sasaki S, Morimoto M, Kawabata K, Ito E, Abe K, Sambongi T. Imaging elastic properties of soft materials immersed in water using force modulation mode in atomic force microscopy. Jpn J Appl Phys 1998;37:3860–3.